CHEMISTRY OF MATERIALS
Cite This: Chem. Mater. 2018, 30, 6744−6755
Article
pubs.acs.org/cm

Highly Stable Perovskite Photodetector Based on Vapor-Processed Micrometer-Scale $CsPbBr_3$ Microplatelets

Ying Li,[†] Zhifeng Shi,*[,†,‡] Lingzhi Lei,[†] Fei Zhang,[†] Zhuangzhuang Ma,[†] Di Wu,[†,‡] Tingting Xu,[†,‡] Yongtao Tian,[†,‡] Yuantao Zhang,[§] Guotong Du,[§] Chongxin Shan,*[,†,‡,∥] and Xinjian Li*[,†,‡]

[†]Department of Physics and Engineering, Zhengzhou University, Kexue Road 100, Zhengzhou 450001, China
[‡]Key Laboratory of Materials Physics of Ministry of Education, Zhengzhou University, Daxue Road 75, Zhengzhou 450052, China
[§]State Key Laboratory on Integrated Optoelectronics, College of Electronic Science and Engineering, Jilin University, Qianjin Street 2699, Changchun 130012, China
[∥]State Key Laboratory of Luminescence and Applications, Changchun Institute of Optics, Fine Mechanics and Physics, Chinese Academy of Sciences, Changchun 130033, China

Supporting Information

ABSTRACT: Recently, halide perovskites have attracted tremendous attention because of their great abilities in large-scale and cost-effective manufacturing of optoelectronic devices. Here, a novel photodetector configuration was proposed by employing vapor-processed micrometer-scale inorganic $CsPbBr_3$ microplatelets as the light absorber. Temperature-dependent steady-state and time-resolved photoluminescence spectra were first recorded to study the emission mechanisms and carrier recombination dynamics of the $CsPbBr_3$ microplatelets. Furthermore, a photoconductive detector was prepared, and the device exhibits good performances with a high on/off photocurrent ratio of 4.6×10^3, a responsivity of ~1.33 A/W, and a specific detectivity of 0.86×10^{12} jones. Additionally, temperature-dependent current−voltage and current−time characteristics of the photodetector were studied to assess the thermal effects on its photodetection ability. In particular, the unencapsulated photodetector demonstrates a prominent stability over the long-term temperature endurance measure in ambient air. Even operated at 373 K, the photodetector can operate properly, showing a high temperature resistance. Moreover, the device performance can almost be retained even with a 7 month storage in air. The experimental results suggest that the $CsPbBr_3$ microplatelets can serve as a good candidate for the fabrication of high-performance photodetectors compatible with practical applications.

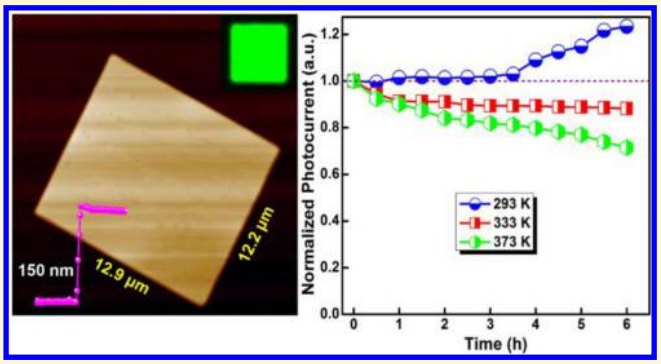

INTRODUCTION

Recently, metal halide perovskites have triggered an increasingly intensive interest owing to their remarkable characteristics, including direct bandgap, tunable emission wavelength, high light absorption coefficient, simple processing technique, and high and well-balanced carrier transport ability.[1−10] These unique features render such perovskite materials promising candidates for optoelectronic device applications such as photovoltaic cells,[11,12] luminescent devices,[13−16] lasing,[17−19] and photodetectors.[4,20−24] However, the study of photodetectors is still short of important breakthroughs that can promote perovskite-based photodetectors into practical applications, which is mainly because of the difficulty in preparing high-quality perovskite light absorbers with a good compactness and a good crystallinity and also the undesired hypersensitivity of perovskites in air with moisture. It is well-known that when organic−inorganic hybrid perovskites are exposed to air ambient, they suffer rapid deterioration. However, inorganic perovskites $CsPbX_3$ show remarkable stability except for all the superior characteristics inherited from the organic−inorganic perovskites, and many reports have argued that $CsPbX_3$ has a high thermal stability until its melting at ~500 °C.[25] Thus, as the alternatives, inorganic perovskites are beginning to draw much scientific attention in reliable photodetector fabrication.[26−31] For instance, Chen et al. demonstrated a simple photodetector using horizontal single-crystal $CsPbX_3$ nanowires with controlled crystallographic orientations as the light absorber, showing an on/off photocurrent ratio of 10^3 and a response time of <0.1 s.[26] Lu et al. reported a $CsPbBr_3$ photodetector integrated with Si nanowires with a responsivity of 54 mA/W and a response time of 0.48/1.03 ms.[22] Zeng and co-workers demonstrated a planar device configuration constructed with $CsPbBr_3$ nanocrystals with a preferred orientation, and the photoresponsivity

Received: June 9, 2018
Revised: September 18, 2018
Published: September 18, 2018

DOI: 10.1021/acs.chemmater.8b02435
Chem. Mater. 2018, 30, 6744−6755

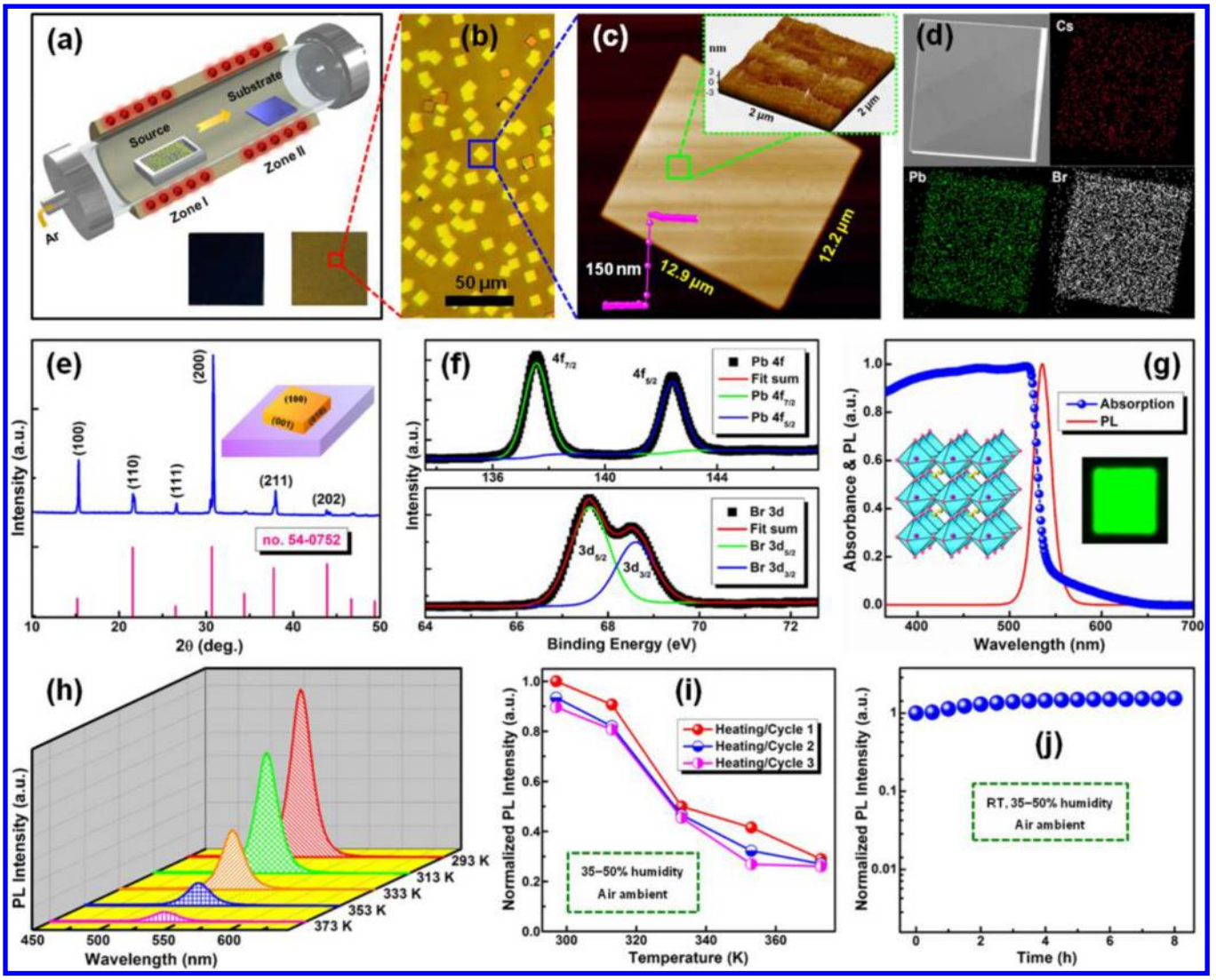

Figure 1. (a) Schematic diagram of the reaction setup for $CsPbBr_3$ microplatelets. (b) Optical microscopy image of the as-prepared $CsPbBr_3$ sample grown on SiO_2/Si substrate. (c) 2D AFM image of a single $CsPbBr_3$ microplatelet. (d) EDS mapping of an individual $CsPbBr_3$ microplatelet showing the uniform distribution of Cs, Pb, and Br elements. (e) XRD spectrum (top) of the $CsPbBr_3$ microplatelets. The bottom pattern shows the standard cubic $CsPbBr_3$ XRD pattern. (f) XPS spectra of Pb 4f and Br 3d of the $CsPbBr_3$ microplatelets. (g) PL and absorption spectra tested at RT. (h) Temperature-dependent emission spectra. (i) Three thermal cycling tests of the $CsPbBr_3$ microplatelets. (j) Photostability test of the $CsPbBr_3$ microplatelets.

and response speed were substantially enhanced by introducing the localized surface plasmonic effect.[28]

Nevertheless, there are many obstacles preventing the further improvement of the detector performance, for example, the presence of a good deal of grain boundaries and defects in nano- or polycrystalline material forms.[32,33] Thus, the photocurrent signal generated in the photodetectors has to preferentially compensate for such undesirable current loss, resulting in a slower photoresponse and a lower photoresponsivity. Moreover, in previous studies, the $CsPbX_3$ light absorbers are often characterized by the high-density and low-size nanocrystallites,[12] which are short of well-defined facets and irregularly stacked. The trap states may exist at the interfacial areas among the nanocrystallites. In this way, the photogenerated carriers can be rapidly trapped. Hence, from the device point of view, it is very essential to further improve the material quality and maintain the integrity of $CsPbX_3$ light absorbers. Besides, in previous studies, the photodetector performance including the photoresponsivity, on/off photocurrent ratio, response time, and other related parameters has always been emphasized, but the critical stability of the unencapsulated device has been rarely studied. For a broader range of applications in low-cost photodetection, investigation of the working stability of the perovskite photodetectors is imperative and should be facilitated.

In this work, we report a vapor-phase approach for the growth of high-quality micrometer-scale inorganic $CsPbBr_3$ microplatelets. A high crystallinity and fewer grain boundaries make the perovskites less susceptible to degradation, resulting in a device with long-term operation stability. Temperature-dependent steady-state and time-resolved photoluminescence (PL) tests were first performed to study the emission mechanisms and carrier recombination dynamics of the high-quality $CsPbBr_3$ microplatelets. Furthermore, a prototypical perovskite photodetector was prepared with a coplanar photoconduction configuration, exhibiting a high on/off ratio of 4.6×10^3, a photoresponsivity of ~1.33 A/W, and a specific detectivity of 0.86×10^{12} jones. More importantly, the working

DOI: 10.1021/acs.chemmater.8b02435
Chem. Mater. 2018, 30, 6744–6755

stability of the device was investigated to prove the sensitivity of the photodetection ability to atmosphere temperature and to evaluate its compatibility for practical applications. The underlying reasons for the photoresponsivity and on/off ratio decays are also discussed briefly. It is reasonably believed that our results may promote the development of stable and efficient perovskite photodetectors suitable for practical applications even under harsh environments.

RESULTS AND DISCUSSION

In this experiment, high-quality micrometer-scale inorganic $CsPbBr_3$ microplatelets were synthesized by using the chemical vapor phase deposition (CVD) technique, in which a double temperature zone tube furnace was employed as the reactor. The corresponding setup diagram is illustrated in Figure 1a, and the detailed synthesis process is shown in the Experimental Section. The inset in Figure 1a presents the photographs of the $CsPbBr_3$ microplatelets grown on the commercially available SiO_2/Si substrate. From the areas marked by a red square, we can see that the microplatelets are characterized by well-defined square shapes with smooth outer surfaces and sharp edges (Figure 1b). Note that the lateral dimension of the $CsPbBr_3$ microplatelets distributes in a range of 7−15 μm with a typical thickness of ∼150 nm. Besides, the produced $CsPbBr_3$ microplatelets present a highly smooth surface, as shown in the two-dimensional (2D) atom force microscopy (AFM) image shown in Figure 1c, and the corresponding surface roughness is about 0.6 nm (inset in Figure 1c), which is perfectly flat in optical level and also is evidence of the highly crystallized nature of $CsPbBr_3$ microplatelets. Energy-dispersive X-ray spectroscopy (EDS) tests were used to study the elemental composition and distribution of an individual $CsPbBr_3$ microplatelet. As displayed in Figure 1d, the Cs, Pb, and Br elements are distributed uniformly across the whole microplatelet and overlay with each other perfectly. Quantitative analysis of the spectrum reveals that the Cs, Pb, and Br elements have an atomic ratio of about 1:1.1:3.2 (Figure S1, Supporting Information), which is close to the stoichiometry of the $CsPbBr_3$ material. In fact, many comparative experiments have been carried out to achieve such high-quality $CsPbBr_3$ microplatelets. Other forms were also prepared at relatively low reaction pressure, such as $CsPbBr_3$ thin films and microwire networks, as presented in Figure S2 (Supporting Information). The morphology dependence of $CsPbBr_3$ products on reaction pressure may be due to their different thermodynamically crystalline process in $CsPbBr_3$ formation. Furthermore, X-ray diffraction (XRD) measurements were used to examine the structural characteristics of $CsPbBr_3$ microplatelets. As shown in Figure 1e, two dominant and characteristic diffraction peaks at 15.34° and 30.81° were clearly observed, corresponding to the (100) and (200) crystalline planes of cubic $CsPbBr_3$ (a = 2.92 Å, JCPDS no. 54-0752). Note that the line width of the (100) diffraction peak is as small as 0.03°, which implies that the $CsPbBr_3$ microplatelets are well-fabricated with a high crystalline quality. The cubic-structured phase and single-crystal nature of the $CsPbBr_3$ microplatelets were further verified by the transmission electron microscopy (TEM) measurements (Figure S3, Supporting Information). The above structural investigation reveals that the microplatelets grow along the [010] and [001] directions and the (100) facet is exposed. We further carried out X-ray photoelectron spectroscopy (XPS) measurements to study the bond states and chemical composition of the as-prepared $CsPbBr_3$ microplatelets. Figure S4 shows the total XPS spectrum of the products, where the signals from Br, Pb, C, and Cs elements are observed above the detection limit. The Pb 4f and Br 3d signals as measured are displayed in Figure 1f. As shown in the upper pane, the binding energies for Pb $4f_{5/2}$ and Pb $4f_{7/2}$ are 139.8 and 135 eV, respectively, which are related to the stoichiometric $CsPbBr_3$, or Pb^{2+} in $PbBr_3^-$.[34] As shown in the bottom pane, a binding energy (65.0 eV) corresponding to Br $3d_{5/2}$ and a splitting corresponding to the Br $3d_{3/2}$ (1.0 eV) can be observed. This component can be assigned to the Br^- state in $CsPbBr_3$.[35] Meanwhile, considering the atomic sensitivity factors and the area of the spectra, the atomic ratio of Pb and Br is approximated to be 1:3.04, matching well with the results in EDS measurements. To investigate the optical quality of the $CsPbBr_3$ microplatelets, PL and absorption spectra were both measured at room temperature (RT, 293 K). Figure 1g shows a highly symmetric PL spectrum peaking at 530 nm with a relatively narrow full-width at half-maximum (fwhm) of 27 nm. The blue line presents the absorption spectra of the $CsPbBr_3$ microplatelets, and a sharp absorption edge occurs at 540 nm, consistent with previous studies.[14,31] The inset in Figure 1g illustrates a typical PL image of a single $CsPbBr_3$ microplatelet, and the green emission is uniformly distributed over the whole microplatelet. In addition, it is noteworthy that the undesirable sub-bandgap emissions caused by the defect states were not detected in the present case. The remarkable optical properties suggest that the $CsPbBr_3$ microplatelets have a low defect density, which is of great importance for their applications as a light absorber in photodetectors. In addition, the emission wavelength of the perovskite microplatelets can be adjusted with different halide composition. As displayed in Figure S5, by mixing the Cl/Br, the emission wavelength of $CsPbBr_{3-x}Cl_x$ ($0 < x < 3$) was adjusted from blue to green emission. By mixing the Br/I, the emission wavelength of $CsPbBr_xI_{3-x}$ ($0 < x < 3$) was adjusted from green to red emission.

To assess the suitability of the as-synthesized $CsPbBr_3$ microplatelets to practical photodetector applications, we performed the thermal cycling PL tests (293−373 K) for the $CsPbBr_3$ microplatelets. Also, the photostability measurements under a continuous light excitation (365 nm) were carried out. As shown in Figure 1h, a series of PL spectra at various ambient temperatures were measured under a constant light excitation and put together for comparison. One can see that the PL intensity decreases gradually with increasing the ambient temperature because of the added nonradiative recombination induced by the well-known heating effect. At 313 K, the emission intensity reduced to 75%, and at 373 K, the PL intensity remains ∼25% of the initial value. Furthermore, we performed three successive thermal cycling tests to study the thermal stability. As shown in Figure 1i, an emission decay of only ∼10% occurs after three heating−cooling cycles, greatly superior to the performance of $CsPbBr_3$ thin films (Figure S6) and other forms.[36,37] To get more convincing conclusions regarding thermal stability of $CsPbBr_3$ microplatelets, 10 successive thermal cycling measurements were further conducted. As presented in Figure S7 (Supporting Information), only a ∼ 20% integrated PL intensity decay was produced after 10 cycles. The results show the reproducible and stable features of the $CsPbBr_3$ light absorber and also its remarkable temperature resistance, opening opportunities for making temperature-stable photodetectors. Moreover, the photostability of the $CsPbBr_3$ microplatelets was investigated

DOI: 10.1021/acs.chemmater.8b02435
Chem. Mater. 2018, 30, 6744−6755

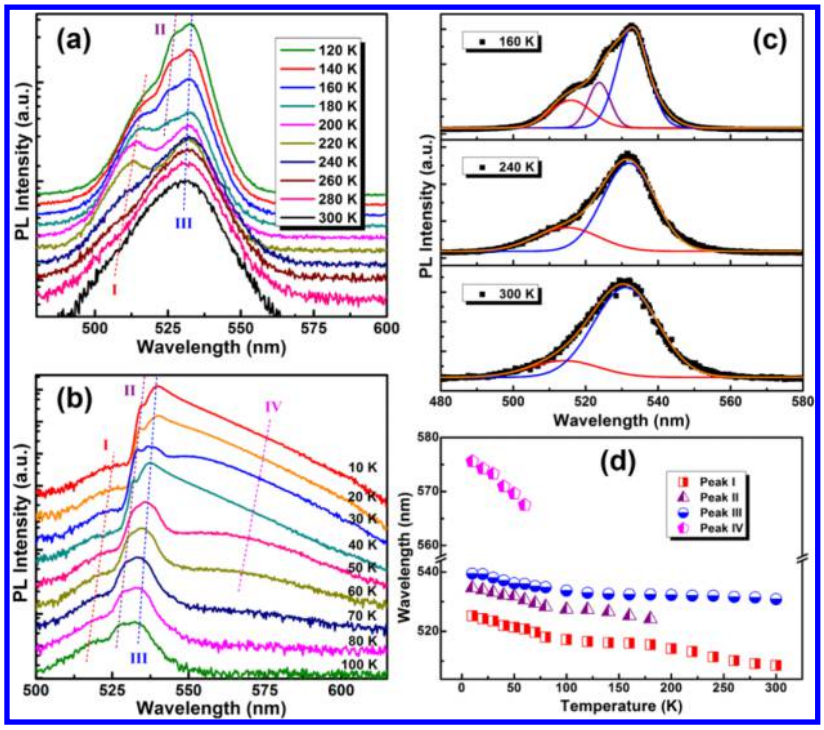

Figure 2. Temperature-dependent PL spectra ranging from (a) 300 to 120 K and (b) 100 to 10 K on a semilogarithmic scale. (c) Gaussian deconvolution measured at 160, 240, and 300 K. (d) Shift of the emission positions of peaks I, II, III, and IV as a function of measured temperature.

by illuminating the sample with a portable ultraviolet lamp at a 10 cm distance. Figure S8 displays a series of PL spectra of the $CsPbBr_3$ microplatelets recorded every 0.5 h. It is unexpectedly yet interesting that a PL enhancement behavior was observed over the test period (8 h), which is presumably related to the "photoactivation" phenomenon as reported in a previous study.[38]

To better understand the optical transition mechanisms of the perovskite microplatelets, the PL measurements were further conducted in the temperature range of 10−300 K. As displayed in Figure 2a,b, the PL spectra at two temperature windows were put together for a clear view of the emission evolution process. At 300 K, one can observe that the PL spectrum is characterized by an intense emission peak at around 530 nm (peak III), accompanied by an imperceptible shoulder at ∼505 nm (peak I). With a decrease of the temperature, the intensity ratio of the two peaks changes. Here, peak III was assigned to the free exciton emission in $CsPbBr_3$ microplatelets. Many reports have indicated that the exciton binding energy of $CsPbBr_3$ is larger than 26 meV, ensuring excitons survival well above RT, which is well consistent with our discussions.[39,40] The relatively weak peak I, which locates at the high-energy side of peak III, may be related with the electron−light hole transition in $CsPbBr_3$, and the previous studies have also reported a similar phenomenon.[41,42] Of course, more work should be done to further investigate the transition mechanisms of peak I. With the further decrease of temperature, the intensity of peaks I and III increases, and their peak positions gradually blue-shift. Herein, we consider that the electron−phonon interaction and the crystal lattice thermal expansion should be responsible for such an uncommon blue-shift phenomenon, and a similar observation has been reported in lead/copper chalcogenide semiconductors.[43] As the temperature decreased to 180 K, a new emission peak appeared at the position of 525 nm (peak II), and this emission component can be retained at the low temperature of 10 K. Du and Shi have performed the density functional theory calculations to determine the origin of the above-bandgap emission in $CsPbBr_3$.[44] The energy level of Br vacancy (V_{Br}) locates above the conduction band of $CsPbBr_3$. Experimentally, Sebastian et al. observed a bound excitonic emission in $CsPbBr_3$ with the energy level located above the free exciton emission.[45] Considering the energy separation between peaks II and III (free excitons), we attributed peak II to V_{Br}-related emission in $CsPbBr_3$ microplatelets. It is noteworthy that another emission component at the long-wavelength side, ∼565 nm (peak IV), appears when the temperature reduces to 60 K, and its intensity proportion increases gradually with decreasing temperature, which may result from the reduction of nonradiative recombination probability at low temperatures. Also, a similar phenomenon has been observed in other studies.[46,47] Therefore, we attributed peak IV to the trapped charge-carrier recombination or trap-mediated radiative recombination. Because of the absence of irregular and/or reversal PL shift, we believe that there is no structural phase transition in the cooling process, unlike previous reports on $CH_3NH_3PbI_3$ systems.[48,49]

The above results on temperature-dependent PL spectra suggest that there are four carrier transition channels in $CsPbBr_3$ microplatelets, and they take effect at different temperature levels. In the 200−300 K temperature window, peak I and III dominate the PL spectra, as displayed clearly by the Gaussian deconvolution of the emission spectra in Figure 2c (300 and 240 K, bottom and middle panes). In the 70−180 K temperature window, peaks I, II, and III contribute the emission spectra, as shown in a Gaussian deconvolution performed at 160 K (upper pane). In the 10−60 K temperature window, peaks I, II, III, and IV constitute the PL spectra together. In Figure 2d, the variation of peak positions for four emission contributors is summarized as a

DOI: 10.1021/acs.chemmater.8b02435
Chem. Mater. 2018, 30, 6744−6755

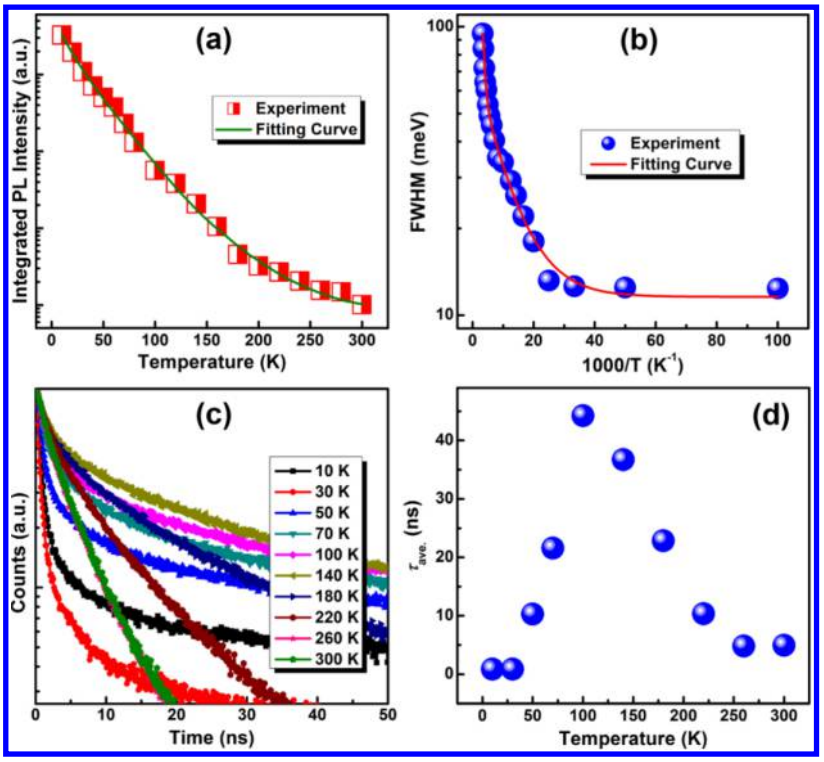

Figure 3. (a) Integrated PL intensity and (b) fwhm of the $CsPbBr_3$ microplatelets versus inverse temperature and the fitted lines. (c) PL decays at different temperature points. (d) Changing trend of τ_{ave} of the $CsPbBr_3$ microplatelets.

function of temperature. From the variation trend of peak III, the temperature sensitivity of the photon energy of $CsPbBr_3$ microplatelets can be estimated according to the empirical equation of $E_T = E_0 + \eta T$, in which E_T and E_0 are the measured photon energy and fitting constant at $T = 0$. Finally, the temperature sensitivity coefficient of $\eta = dE/dT$ was estimated to be 0.316 ± 0.007 meV/K.

Because the cubic phase of $CsPbBr_3$ microplatelets is stable in the temperature range, important parameters like exciton binding energy (E_b) and exciton−phonon interaction are estimated using the data procured above. As shown in Figure 3a, the intensity of peak III (exciton-related emission) as a function of temperature is plotted to determine the E_b. One can see that the integrated PL intensity increases exponentially with decreasing temperature owing to the thermally activated nonradiative recombination process, and eq 1 was used to describe such temperature quenching behavior[50]

$$I(T) = \frac{I_0}{1 + A\exp\left(-\frac{E_b}{KT}\right)} \quad (1)$$

where A is a proportional constant, I_0 the PL intensity at 0 K, and K the Boltzmann constant. The value of E_b is 31.6 ± 1.3 meV, slightly larger than the RT thermal ionization energy. In addition, the fwhm of the PL emission of $CsPbBr_3$ microplatelets is fitted to investigate the exciton−phonon interaction in the carrier transition process as presented in Figure 3b, and the data are fitted using the equation[51]

$$\Gamma(T) = \Gamma_0 + \sigma T + \frac{\Gamma_{op}}{\exp(\hbar\omega_{op}/KT) - 1} \quad (2)$$

in which σ and Γ_{op} are the exciton−acoustic phonon interaction and the exciton−optical phonon contribution to the line width broadening; $\hbar\omega_{op}$ and Γ_0 represent optical phonon energy and the inhomogeneous broadening contribution. It can be seen that Γ_0 is the main contributor to the formula at the low-temperature level, whereas σ and Γ_{op} dominate the formula at the high-temperature level. Thus, the value of fwhm would rise with temperature nonlinearly. Based on the fitting results, one conclusion that could be made is that the optical phonon is involved in the exciton−phonon interaction mainly. Accordingly, the values of $\hbar\omega_{op}$ and Γ_{op} were estimated to be 32.8 ± 1.9 and 66.9 ± 3.2 meV, respectively, implying a strong interaction between exciton and optical phonon and agreeing well with the thermal antiquenching effect of $CsPbBr_3$ microplatelets at high temperature.

Furthermore, temperature-dependent transient PL tests were studied to understand the carrier recombination dynamics. Figure 3c displays a series of PL decay curves at 10 representative temperature points, which can be well-fitted with the biexponential decays[52]

$$A(t) = A_1\exp\left(-\frac{t}{\tau_1}\right) + A_2\exp\left(-\frac{t}{\tau_2}\right) \quad (3)$$

in which A_1 and A_2 are the distribution coefficients and τ_1 and τ_2 stand for the characteristic PL decay lifetimes. The average lifetime (τ_{ave}) is evaluated with the A_i and τ_i values according to the expression of $\tau_{ave} = (A_1\tau_1^2 + A_2\tau_2^2)/(A_1\tau_1 + A_2\tau_2)$, and the obtained τ_{ave} values are summarized in Figure 3d. One can observe that the τ_{ave} increases gradually as the temperature increases below 100 K and then decreases significantly. We can infer from previous research that the lengthening of τ_{ave} at elevated temperatures may be due to the introduction of charge carrier trapping or localized states as the relaxation pathways.[53] Besides, the interaction between excitons and trap

DOI: 10.1021/acs.chemmater.8b02435
Chem. Mater. 2018, 30, 6744−6755

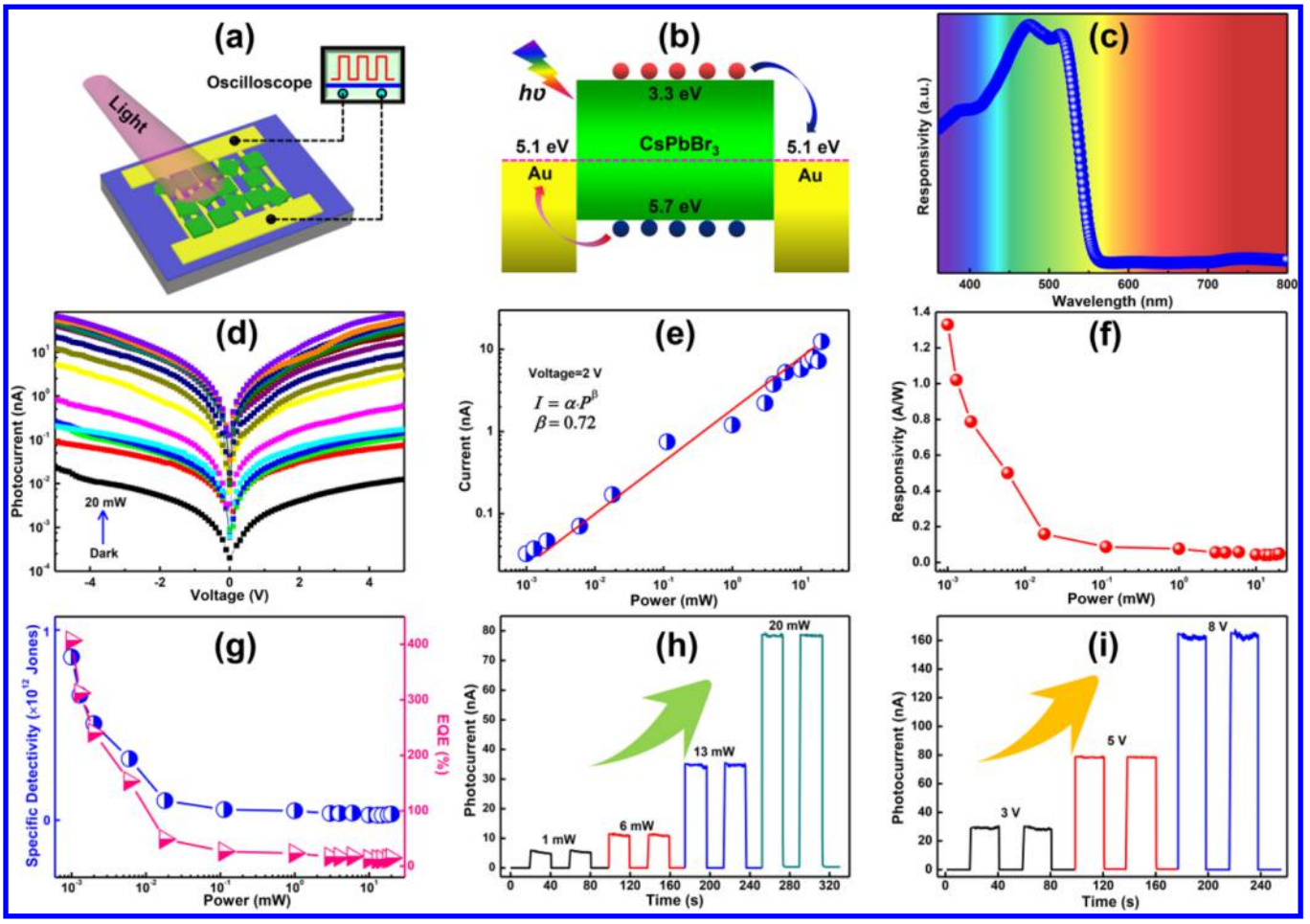

Figure 4. (a) Schematic diagram of the photodetector based on the $CsPbBr_3$ microplatelets. (b) Energy band alignment of the Au/$CsPbBr_3$/Au structure. (c) Spectral response of the $CsPbBr_3$ microplatelets photodetector. (d) $I-V$ curves with different light irradiation intensities. (e) Logarithmic plot of the photocurrent versus light irradiation power at a bias of 2 V. (f) Photoresponsivity, (g) specific detectivity, and EQE versus light irradiation power. $I-t$ curves operated at different (h) bias voltage and (i) light irradiation power.

states with rising temperature will induce the increase of PL lifetime. As for the subsequent decrease of τ_{ave} (100 K and above), the thermal degradation of $CsPbBr_3$ microplatelets at high temperatures deserves concern because the formation of added nonradiative recombination centers is inevitable.

To prove the potential applications of the $CsPbBr_3$ microplatelets in a photoelectric device, a photodetector device was prepared with a metal−semiconductor−metal configuration, and the corresponding device structure is shown in Figure 4a. Figure 4b shows the energy band diagram of the Au/$CsPbBr_3$/Au structure, in which E_C and E_V indicate the conduction band minimum and valence band maximum of the $CsPbBr_3$, respectively. When irradiated by the light source (405 nm in present case), electron−hole pairs are produced because of the photoelectric effect. Under the applied electric field, the carriers are separated rapidly and collected by opposite contact electrodes. Thus, the $CsPbBr_3$ microplatelets photodetectors could operate effectively, and accordingly, the photocurrent gradually increases with electric field intensity and light illumination. Figure 4c demonstrates the spectral response of the device, and a good spectral selectivity is well consistent with the absorption result shown above. Furthermore, the light intensity-dependent photoresponse performance of the studied photodetector was studied by changing the incident light intensity from the dark to 20 mW, and the corresponding current−voltage ($I-V$) characteristics are depicted in Figure 4d. One can see that the photocurrent is highly dependent on the light intensity and increases gradually with increasing light intensity, which may be because the amount of photogenerated electron−hole pairs is proportional to the absorbed photon flux. Additionally, some $I-V$ characteristic curves are featured by an asymmetrical behavior, which is probably because of the undesirable interface states at the Au/$CsPbBr_3$ interface. Note that the studied $CsPbBr_3$ microplatelets photodetector presents a low dark current of 1.73×10^{-11} A at 5.0 V, and the photocurrent increases several orders of magnitude to a value of 7.89×10^{-8} A at the illumination power of 20 mW. Thus, an on/off photocurrent ratio of 4.56×10^3 is achieved. In addition, the relationship between photocurrent (I_p) and the light excitation power was fitted by the power law of $I_p = \alpha \cdot P^{\beta}$, in which α represents a proportional constant, P is the light excitation power, and β is an exponent associated with its photoresponse corresponding to the light intensity. As shown in Figure 4e, the fitting curve produces a sublinear relationship of $\beta = 0.72$. This fractional power dependence ($0.5 < \beta < 1.0$) has also been found in other photodetectors and probably results from the complex process of electron−hole generation, recombination, and trapping in a semiconductor.[23] Besides, other key device parameters—photoresponsivity (R), specific detectivity (D^*)

DOI: 10.1021/acs.chemmater.8b02435
Chem. Mater. 2018, 30, 6744−6755

Table 1. Summary of the Performance of the Perovskite-Based Photodetectors

active materials	responsivity (A/W)	D^* ($\times 10^9$ jones)	EQE (%)	on/off ratio	ref
$CH_3NH_3PbI_3$ single crystals	2.531	–	396.2	–	54
$CH_3NH_3PbBr_3$ single crystals	0.012	–	3.17	–	55
$CH_3NH_3PbI_3$ films	0.49×10^{-6}	–	–	70	56
$CH_3NH_3PbBr_{3-x}I_x$ films	0.055	–	–	$\sim 10^3$	57
$CH_3NH_3PbI_3$ nanowire	0.1	1020	–	340	58
$CH_3NH_3PbI_3$ microwire	1.32	2500	–	23	59
$CH_3NH_3PbBr_3$ nanowire	–	–	61.9	62	60
$CsPbBr_3$ nanosheets	0.64	–	54	$\sim 10^3$	30
$CsPbBr_3$ nanocrystals	0.01	1.684	8	$\sim 10^5$	61
$CsPbBr_xI_{3-x}$ nanocrystals	>1.0	–	–	$\sim 10^4$	62
$CsPbBr_3$ microcrystals	2.1	–	485	$\sim 10^3$	63
$CsPbBr_3$ microparticles	0.18	–	42	8.0×10^3	64
$CsPbBr_3$ microplatelets	1.33	1800	407	4.6×10^3	this work

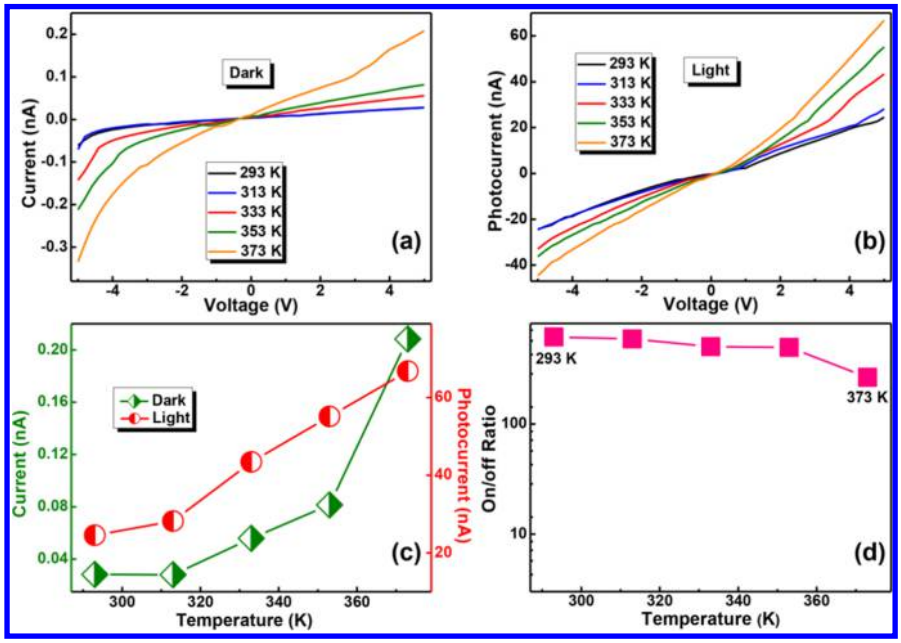

Figure 5. $I-V$ characteristics of the photodetector (a) in dark conditions and (b) under light irradiance with different temperature conditions. (c) Variation of the dark current and photocurrent of the photodetector at different temperature points (5 V, 6 mW). (d) Variation of the on/off current ratio of the $CsPbBr_3$ microplatelets photodetector at different temperature points.

and external quantum efficiency (EQE)—were examined to quantitatively evaluate its photoresponse ability. R is defined by the equation $R = (I_p - I_d)/P_{opt}{\cdot}S$, where I_d and P_{opt} stand for the dark current and the incident light intensity, respectively, and S is the active area. Figure 4f presents the photoresponsivity curve versus the incident light power, and a maximum value of 1.33 A/W was achieved under a low light excitation power of 1 μW. The undesired saturation at high light illumination power may be related with the photocurrent saturation, which results from the filling mechanism of the sensitizing centers in $CsPbBr_3$ microplatelets at high light illumination intensity. As presented in Figure 4g, the D^* and EQE were also calculated and plotted with the incident light illumination power using the following relations:

$$D^* = \frac{(A{\cdot}f)^{1/2}}{\mathrm{NEP}} \tag{4}$$

$$\mathrm{NEP} = \frac{(\overline{i_n^2})^{1/2}}{R} \tag{5}$$

$$\mathrm{EQE} = \frac{I_p/e}{P_{opt}/h\nu} = R\frac{hc}{e\lambda} \tag{6}$$

in which A represents the effective area of the sample; NEP is the noise equivalent power; f is the electrical bandwidth; $(\overline{i_n^2})^{1/2}$ is the root-mean-square value of the noise current acquired by using a lock-in amplifier at different frequencies; λ is the light wavelength, and h and c stand for Planck's constant and light speed. Figure S9 presents the relationship of $(\overline{i_n^2})^{1/2}$ with the frequency, from which the noise level per unit bandwidth (1 Hz) of the photodetector was measured to be 0.76 pA $Hz^{1/2}$. Then, the value of D^* was calculated and plotted with light illumination intensity. Both parameters display almost the same evolution trend as photoresponsivity, with the highest values of 0.86×10^{12} jones and 407% at the incident illumination power of 1 μW, which are much better than many reported results based on lead halide perovskites, as seen in Table 1.

DOI: 10.1021/acs.chemmater.8b02435
Chem. Mater. 2018, 30, 6744−6755

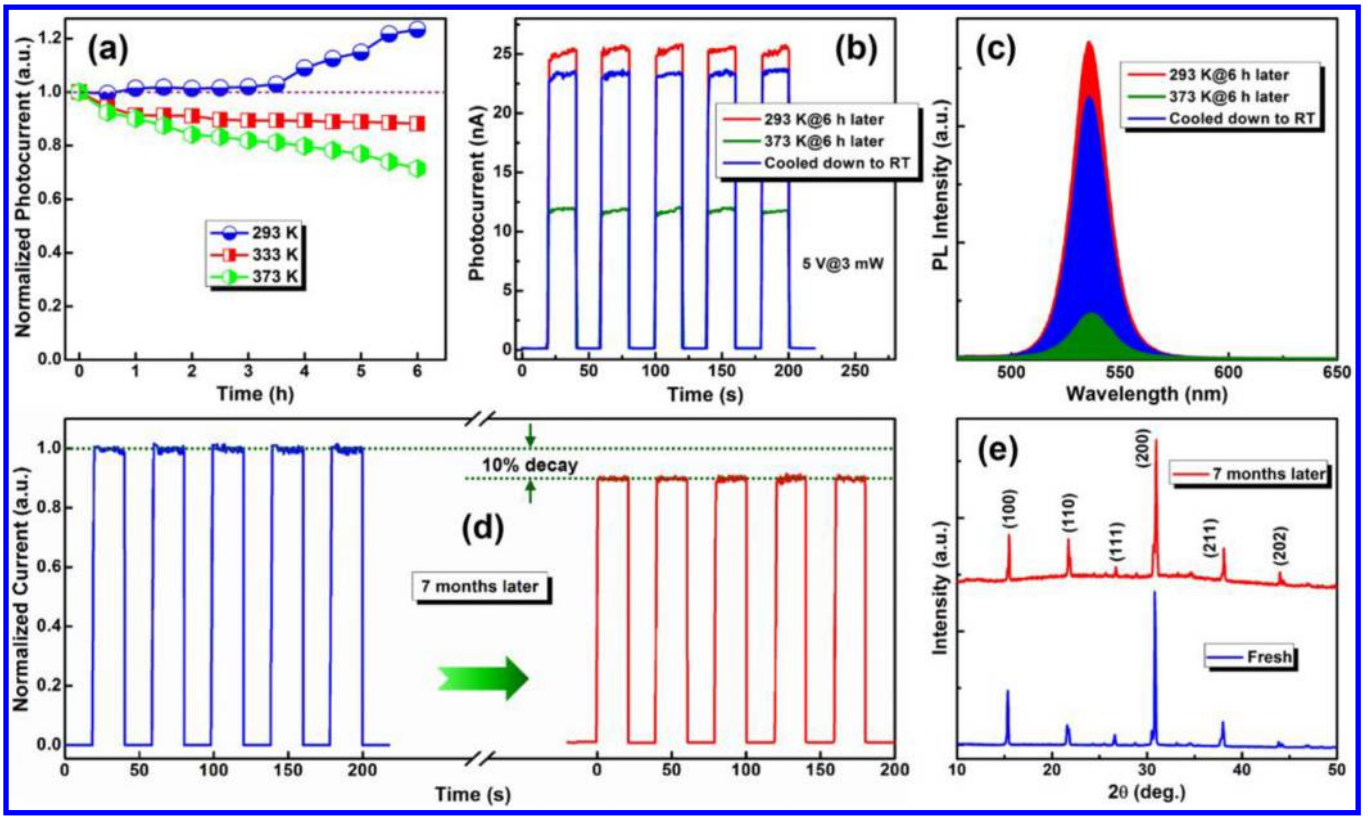

Figure 6. (a) Normalized photocurrent of the unencapsulated $CsPbBr_3$ microplatelets photodetector versus running time at 293, 333, and 373 K. (b) Temporal photoresponse curves of the device after aging for 6 h at 293 and 373 K and after naturally cooling to RT. (c) PL spectra of the $CsPbBr_3$ microplatelets after aging for 6 h at 293 and 373 K and after naturally cooling to RT. (d) Long-term storage stability. The last five cycles are the photoresponse after storage in air for 7 months. (e) Comparison of the XRD patterns of the $CsPbBr_3$ microplatelets before and after storage for 7 months in ambient air.

Temporal photoresponse is also an important performance parameter for the photodetectors. The current−time (I−t) curves of the device versus bias voltage were therefore measured to examine the time response, where the pulse bandwidth of the excitation light was fixed at 20 s per cycle and the illumination was switched on and off at different bias voltages (3, 5, and 8 V). As presented in Figure 4h, the current reversibly switches between low and high conductance with good stability and reproducibility, producing a series of tunable on/off photocurrent ratios. Furthermore, using the photocurrent response recorded at 8 V, the photoresponse time (rise time and fall time), which are the key evaluation criteria for detection performance, are obtained to be 20.9 and 24.6 ms, as displayed in Figure S10. As for the relatively slow response speed, two possible reasons should be considered. First, in our case, the $CsPbBr_3$ microplatelets were dispersed in toluene and then transferred to the SiO_2/Si substrate with Au patterned fingers. Therefore, inevitable interface defects may exist between $CsPbBr_3$ microplatelets and the Au electrode. Second, during the device testing, the incident light is radiated from the upper portion onto the photodetector, that is, on the top of the $CsPbBr_3$ microplatelets. Owing to the relatively large thickness of about 150 nm, the photogenerated carriers need more time to travel through the microplatelets to the underlying Au electrode, resulting in a relatively slow response time. In addition, the photoresponse with different light irradiance powers at 5 V was also studied. As displayed in Figure 4i, the photocurrent increases gradually with rising irradiance power, and the reproducible and prompt photocurrent response also indicates a good cycling stability. In addition to the visible light detection, the photodetector is also sensitive to ultraviolet light. Figure S11 displays the corresponding I−V curves and time-dependent photoresponse of the device under 265 nm light illumination. Similarly, the current can reversibly switch between low and high conductance when the light irradiance was turned on and off, demonstrating a remarkable stability and reproducibility.

It is well-known that the working stability is a challenging issue for perovskite-based photodetectors.[65] In actual application, the photodetector has to be operated in the open air with inconsistent conditions. Therefore, the working stability for the studied photodetector without encapsulation was further investigated at different ambient temperatures to evaluate its temperature tolerance, and the corresponding I−V curves in dark conditions and under light illumination (405 nm, 6 mW) were measured. As shown in Figure 5a, one can observe that the dark current increases gradually with increasing ambient temperature, which can be well-fitted by the following Arrhenius equation:

$$A = A_0 \exp\left(-\frac{E_a}{KT}\right) \tag{7}$$

where A_0 is a proportional constant and K and T are the Boltzmann constant and temperature, respectively. The fitting curve yields the activation energy of $E_a \approx 0.27 \pm 0.08$ eV. For perovskites, the temperature-dependent current increase may be caused by the ion migration, generating halide vacancy defects. Mizusaki and co-workers have experimentally con-

DOI: 10.1021/acs.chemmater.8b02435
Chem. Mater. 2018, 30, 6744−6755

firmed that the activation energy for the migration of Br^- in $CsPbBr_3$ is about 0.25 eV,[66] and the material becomes more conducting with the increase of temperature, well consistent with the results in our case. Of course, the thermally activated process for increased carriers in $CsPbBr_3$ microplatelets is an indisputable fact, similar to traditional semiconductors. Under the light illumination, the $I-V$ curves display the same dependence on ambient temperature as that of the dark current. Typically, at a bias of 5 V, the photocurrent increases from 20 nA at RT to 62 nA at 373 K. Figure 5c summarizes the variation of dark current and photocurrent of the photodetector at different temperature points. As presented in Table S1, the increasing rate of dark current from 293 to 373 K is 6.83, while the decreasing rate of on/off ratio (I_{light}/I_{dark}) from 293 to 373 K is 2.33. Obviously, the decreasing rate of I_{light}/I_{dark} is smaller than the increasing rate of dark current. If the reduction of I_{light}/I_{dark} ratio is just due to the increase of dark current, the changing rate of the two parameters should be equal. Therefore, we consider that other positive factors may exist, which compensate for the I_{light}/I_{dark} ratio. For instance, the elevated ambient temperature could provide energy for the separation of electrons and holes; the increased charge carrier density at high temperature could lower the effective energy barrier height. The above two factors favor an easier carrier transport and contribute to an enhancement in photoconductivity. To further investigate the temperature resistance of the proposed photodetector, temperature-dependent $I-t$ curves of the device on a semilogarithmic scale were measured, in which the bias voltage and light illumination were fixed 5 V and 6 mW, respectively. As shown in Figure S12, the dark current and photocurrent increase simultaneously with temperature as observed in Figure 5c. Even at a high ambient temperature of 373 K, the $CsPbBr_3$ microplatelets photodetector can operate well, demonstrating a reproducible and stable response to on/off cycles. The results show that the photodetector has a remarkable temperature resistance, suggesting $CsPbBr_3$ microplatelets are potentially compatible with practical applications even in harsh environments. No study about the high-temperature working ability of perovskite-based photodetectors has been reported to date, making our study original and useful for progressing to a practical photodetector. Based on the obtained data from temperature-dependent $I-t$ curves, the on/off ratio at different temperatures was calculated and is summarized in Figure 5d. One can see that the on/off photocurrent ratio exhibits a slight decay of ∼16% at 353 K. As the ambient temperature is increased to 373 K, the on/off current ratio decreases by 43%. Despite this, the photodetection ability of such a photodetector can be efficiently sustained. We therefore attribute this decrease of on/off ratio to the increased defect states caused by the thermal effect, by which the photogenerated carriers are quickly trapped. In addition, the photoresponsivity and noise current of the photodetector at different temperature points were also evaluated. As shown in Figure S13, some distinct but regular changing trends are revealed. The photoresponsivity and noise current increase simultaneously with temperature.

To illuminate the long-term working stability of the studied photodetector, the aging test was performed at three representative temperature points (293, 333, and 373 K) under ambient air conditions. The photocurrent of the device without encapsulation versus the running time was performed at fixed bias voltage (5 V) and light excitation power (3 mW). An interesting phenomenon was observed in Figure 6a: the photocurrent recorded at 293 K displays an increasing trend over the whole test period (6 h), which may be due to the "photoactivation" behavior as observed in photostability measurements of the $CsPbBr_3$ microplatelets. Presumably, the photoactivation behavior favors the removal of dangling bonds or undesirable surface states by highly energetic photons; thus, the transport ability of carriers could be improved to some extent. Of course, the heating effect at such a temperature level is insufficient to produce an increase of structural defects that benefit the trap states formation in perovskites. Correspondingly, the dark current of the device over a 6 h running time (Figure S14) does not display an obvious change except for a slight fluctuation. Therefore, the phenomenon of ion migration could be ruled out in our case. As the ambient temperature is elevated to 333 K, an undesired photocurrent decay of ∼10% occurs. When the ambient temperature is further increased to 373 K, the decay magnitude of the photocurrent increases accordingly, and a decay value of ∼33% is produced after 6 h of continuous operation. The corresponding temporal photoresponse curves of the device after aging for 6 h at 293 and 373 K are presented in Figure 6b, and the significantly reduced photocurrent is well consistent with the above discussion. It is understandable that the heating effect would increase with the ambient temperature and running time of the device. Still, the temperature resistance in our study is quite superior to that of other reports.[67,68] An additional and very important observation is that such a photocurrent decay is recoverable; after cooling to RT, the photocurrent (blue line, Figure 6b) could recover to 92% of the initial level. The above studies prove the stable and recoverable performance of the $CsPbBr_3$ microplatelets photodetector even operated at high temperatures, motivating the existing applications and suggesting additional potential applications. To better understand the temperature resistance of $CsPbBr_3$ microplatelets, we recorded the PL spectra after aging for 6 h at 293 and 373 K and after being cooled to RT naturally. As displayed in Figure 6c, the effective PL emission can be sustained even after a 6 h aging test at 373 K except for a substantially reduced PL intensity compared with the counterpart recorded at 293 K (after 6 h of aging), which implies that the optical performance of the $CsPbBr_3$ microplatelets suffers from a degradation owing to the activation of added nonradiative pathways at higher temperature. However, what is exciting is that such a PL emission decay is just a transient behavior. After the sample is naturally cooled to RT, the PL performance recovers to >90% of its original value. Therefore, in terms of the material stability only, the $CsPbBr_3$ microplatelets demonstrate an obvious and impressive advantage compared with other perovskite material systems. Maybe this is the essential reason that ensuring the remarkable temperature resistance of the studied photodetector even worked in the open air and without encapsulation.

Moreover, the long-term storage stability of the present photodetector was studied. As presented in Figure 6d, the last five cycles correspond to the temporal photoresponse curve of the photodetector after seven months of storage in air ambient conditions, without any encapsulation and protection. One can see that the device can still work properly and maintains its photodetection ability except for a slight photocurrent decay of about 10%, obviously better than the devices constructed with hybrid perovskite photodetectors with poor material stability.[69] Figure 6e shows the XRD patterns of the $CsPbBr_3$ micro-

DOI: 10.1021/acs.chemmater.8b02435
Chem. Mater. 2018, 30, 6744−6755

platelets before microplatelets before and after seven months of storage to demonstrate their environmental stability. It can be observed that all the diffraction peaks belong to the cubic $CsPbBr_3$, and no other diffraction signals were found except for the slight change of the peak intensity, suggesting that the $CsPbBr_3$ microplatelets have the ability to maintain the phase purity for seven months of storage. The good material stability together with the remarkable device performance imply that the $CsPbBr_3$ microplatelets are reliable and effective materials for photodetector applications.

CONCLUSION

We have successfully demonstrated a novel configuration of photodetectors by using vapor-processed micrometer-scale inorganic $CsPbBr_3$ microplatelets as the light absorber. Temperature-dependent and time-resolved PL measurements were first performed to study the emission mechanisms and carrier recombination dynamics of the $CsPbBr_3$ microplatelets. Photoresponse analysis reveals that the device possesses a stable and repeatable photocurrent response, and a high on/off ratio of 4.5×10^3, a responsivity of 1.33 A/W, and a specific detectivity of 0.86×10^{12} jones were achieved in the prepared $CsPbBr_3$ microplatelets photodetector. In addition, the unencapsulated photodetector demonstrates an excellent working stability against oxygen and water degradation over the temperature endurance test, and the photodetection ability can be efficiently sustained at 373 K, indicating a good temperature resistance and a desired compatibility for practical applications under harsh environments. The underlying reasons of remarkable working stability have been studied on the basis of thermal cycling and long-term PL measurements of $CsPbBr_3$ microplatelets. This work demonstrates that vapor-processed micrometer-scale $CsPbBr_3$ microplatelets are attractive candidates to be applied in stable and high-performance photodetectors.

EXPERIMENTAL SECTION

Synthesis of $CsPbBr_3$ Microplatelets. In the experiments, commercially available SiO_2/Si template was used as the substrate, and argon was used as the carrier gas. Particularly, a mixture of CsBr and $PbBr_2$ powders with a molar ratio of 1:2 was used as the precursors, which was heated in temperature zone I of the tube furnace at 580 °C. The precleaned SiO_2/Si substrate was located at the center of temperature zone II, and the corresponding temperature was set at 360 °C. After the furnace was heated to the preset temperature, the argon flow rate was set at 100 sccm, and the internal pressure was fixed at 180 Torr. The typical growth time for the $CsPbBr_3$ products was 20 min.

Device Preparation. The $CsPbBr_3$ microplatelets photodetector device was fabricated to investigate their optoelectronic applications. The $CsPbBr_3$ microplatelets dispersed in toluene were sonically agitated for 10 s and then drop-casted onto the SiO_2/Si substrate with Au patterned fingers (note that Au contact electrodes fingers were 5 μm wide and 360 μm long, and the channel spacing is 5 μm). Finally, the samples were annealed at 60 °C for 10 min on a hot plate to decrease the contact resistance and increase the contact adhesion.

Characterizations. *Materials.* Scanning electron microscopy (SEM) (Jeol-7500F, 15 keV) was used to study the microstructures. AFM (Dimension Icon, Bruker) was performed to research the thickness and surface roughness. XRD (Panalytical X'Pert Pro) was performed to study the crystallinity. The EDS attached SEM was used to investigate the element compositions of the products. The crystal structure of the as-synthesized $CsPbBr_3$ microplatelets was analyzed using TEM with a JEM-3010 electron microscope. XPS was performed with a SPECS XR50 system with Mg Kα (1254 eV, width 0.7 eV) as the X-ray source. The absorption of the $CsPbBr_3$ microplatelets was measured using a Shimadzu UV-3150 spectrophotometer. The steady-state PL spectra were recorded by a double-grating spectrofluorometer (Horiba; Fluorolog-3) equipped with a digital temperature controller (LakeShore-325) and a closed-cycle helium cryostat (Jannis CCS-100). The time-resolved PL was tested by a lifetime measurement system with a pulsed LED (Horiba; 371 nm, pulse duration: 1.4 ns) as the light source. Optical images were captured by a Leica SP2 instrument.

Devices. The electrical and optoelectrical measurements of the device were performed by a system that combines a semiconductor characterization system (Keithley 4200-SCS), light sources, a monochromator, an oscilloscope (Tektronix, DPO2012B), and an optical chopper (SRS, SR540) in air ambient. For temperature-dependent optoelectrical measurements, the photodetector was installed on a ceramic heating plate, and the operation temperature could be adjusted from RT to 443 K with a precision of 0.5 K.

ASSOCIATED CONTENT

Supporting Information

The Supporting Information is available free of charge on the ACS Publications website at DOI: 10.1021/acs.chemmater.8b02435.

Additional experimental data as described in the text (PDF)

AUTHOR INFORMATION

Corresponding Authors

*E-mail: shizf@zzu.edu.cn.
*E-mail: cxshan@zzu.edu.cn.
*E-mail: lixj@zzu.edu.cn.

ORCID

Zhifeng Shi: 0000-0002-9416-3948

Notes

The authors declare no competing financial interest.

ACKNOWLEDGMENTS

This work was supported by the National Natural Science Foundation of China (Nos. 11774318, 11604302, 61176044, 11504331, and 51771276), the China Postdoctoral Science Foundation (2015M582193 and 2017T100535), the Science and Technology Research Project of Henan Province (162300410229), the Postdoctoral Research Sponsorship in Henan Province (2015008), and the Outstanding Young Talent Research Fund of Zhengzhou University (1521317001).

REFERENCES

(1) Dong, R.; Fang, Y. J.; Chae, J.; Dai, J.; Xiao, Z. G.; Dong, Q. F.; Yuan, Y. B.; Centrone, A.; Zeng, X. C.; Huang, J. S. High-Gain and Low-Driving-Voltage Photodetectors Based on Organolead Triiodide Perovskites. *Adv. Mater.* **2015**, *27*, 1912−1918.

(2) Zhang, X. Y.; Sun, C.; Zhang, Y.; Wu, H.; Ji, C. Y.; Chuai, Y. H.; Wang, P.; Wen, S. P.; Zhang, C. F.; Yu, W. W. Bright Perovskite Nanocrystal Films for Efficient Light-Emitting Devices. *J. Phys. Chem. Lett.* **2016**, *7*, 4602−4610.

(3) Murali, B.; Saidaminov, M. I.; Abdelhady, A. L.; Peng, W.; Liu, J. K.; Pan, J.; Bakr, O. M.; Mohammed, O. F. Robust and Air-Stable Sandwiched Organo-Lead Halide Perovskites for Photodetector Applications. *J. Mater. Chem. C* **2016**, *4*, 2545−2552.

(4) Pan, W. C.; Wu, H.; Luo, J.; Deng, Z. Z.; Ge, C.; Chen, C.; Jiang, X. W.; Yin, W. J.; Niu, G. D.; Zhu, L.; Yin, L.; Zhou, Y.; Xie, Q. G.; Ke, X.; Sui, M.; Tang, J. $Cs_2AgBiBr_6$ Single-Crystal X-ray Detectors with a Low Detection Limit. *Nat. Photonics* **2017**, *11*, 726−732.

DOI: 10.1021/acs.chemmater.8b02435
Chem. Mater. 2018, 30, 6744−6755

(5) Shi, Z.; Li, Y.; Zhang, Y. T.; Chen, Y. S.; Li, X.; Wu, D.; Xu, T.; Shan, C.; Du, G. High-Efficiency and Air-Stable Perovskite Quantum Dots Light-Emitting Diodes with an All-Inorganic Heterostructure. *Nano Lett.* **2017**, *17*, 313−321.
(6) Song, J. Z.; Li, J. H.; Li, X. M.; Xu, L. M.; Dong, Y. H.; Zeng, H. B. Quantum Dot Light-Emitting Diodes Based on Inorganic Perovskite Cesium Lead Halides ($CsPbX_3$). *Adv. Mater.* **2015**, *27*, 7162−7167.
(7) Sutter-Fella, C. M.; Li, Y. B.; Amani, M.; Ager, J. W.; Toma, F. M.; Yablonovitch, E.; Sharp, L. D.; Javey, A. High Photoluminescence Quantum Yield in Band Gap Tunable Bromide Containing Mixed Halide Perovskites. *Nano Lett.* **2016**, *16*, 800−806.
(8) Xing, J.; Yan, F.; Zhao, Y.; Chen, S.; Yu, H.; Zhang, Q.; Zeng, R. G.; Demir, H. V.; Sun, X. W.; Huan, A.; Xiong, Q. H. High-Efficiency Light-Emitting Diodes of Organometal Halide Perovskite Amorphous Nanoparticles. *ACS Nano* **2016**, *10*, 6623−6630.
(9) Bai, Z. L.; Zhong, H. Z. Halide Perovskite Quantum Dots: Potential Candidates for Display Technology. *Sci. Bull.* **2015**, *60*, 1622−1624.
(10) Veldhuis, S. A.; Boix, P. P.; Yantara, N.; Li, M. J.; Sum, T. C.; Mathews, N.; Mhaisalkar, S. G. Perovskite Materials for Light-Emitting Diodes and Lasers. *Adv. Mater.* **2016**, *28*, 6804−6834.
(11) Tiep, N. H.; Ku, Z. L.; Fan, H. J. Recent Advances in Improving the Stability of Perovskite Solar Cells. *Adv. Energy Mater.* **2016**, *6*, 1501420.
(12) Liang, J.; Wang, C. X.; Wang, Y. R.; Xu, Z. R.; Lu, Z. P.; Ma, Y.; Zhu, H. F.; Hu, Y.; Xiao, C. C.; Yi, X.; Zhu, G. Y.; Lv, H. L.; Ma, L. B.; Chen, T.; Tie, Z. X.; Jin, Z.; Liu, J. All-Inorganic Perovskite Solar Cells. *J. Am. Chem. Soc.* **2016**, *138*, 15829−15832.
(13) Ling, Y. C.; Tian, Y.; Wang, X.; Wang, J. C.; Knox, J. M.; Perez-Orive, F.; Du, Y. J.; Tan, L.; Hanson, K.; Ma, B. W.; Gao, H. W. Enhanced Optical and Electrical Properties of Polymer-Assisted All-Inorganic Perovskites for Light-Emitting Diodes. *Adv. Mater.* **2016**, *28*, 8983−8989.
(14) Yantara, N.; Bhaumik, S.; Yan, F.; Sabba, D.; Dewi, H. A.; Mathews, N.; Boix, P. P.; Demir, H. V.; Mhaisalkar, S. Inorganic Halide Perovskites for Efficient Light-Emitting Diodes. *J. Phys. Chem. Lett.* **2015**, *6*, 4360−4364.
(15) Li, G. R.; Rivarola, F. W. R.; Davis, N. J. L. K.; Bai, S.; Jellicoe, T. C.; Pena, F. D. L.; Hou, S. C.; Ducati, C.; Gao, F.; Friend, R. H.; Greenham, N. C.; Tan, Z. K. Highly Efficient Perovskite Nanocrystal Light-Emitting Diodes Enabled by a Universal Crosslinking Method. *Adv. Mater.* **2016**, *28*, 3528−3534.
(16) Jin, X. C.; Zhang, X. J.; Fang, H.; Deng, W.; Xu, X. Z.; Jie, J. S.; Zhang, X. H. Facile Assembly of High-Quality Organic-Inorganic Hybrid Perovskite Quantum Dot Thin Films for Bright Light-Emitting Diodes. *Adv. Funct. Mater.* **2018**, *28*, 1705189.
(17) Li, M. J.; Wei, Q.; Muduli, S. K.; Yantara, N.; Xu, Q.; Mathews, N.; Mhaisalkar, S. G.; Xing, G. C.; Sum, T. C. Enhanced Exciton and Photon Confinement in Ruddlesden-Popper Perovskite Microplatelets for Highly Stable Low-Threshold Polarized Lasing. *Adv. Mater.* **2018**, *30*, 1707235.
(18) Zhou, H.; Yuan, S. P.; Wang, X. X.; Xu, T.; Wang, X.; Li, H. L.; Zheng, W. H.; Fan, P.; Li, Y. Y.; Sun, L.; Pan, A. L. Vapor Growth and Tunable Lasing of Band Gap Engineered Cesium Lead Halide Perovskite Micro/Nanorods with Triangular Cross Section. *ACS Nano* **2017**, *11*, 1189−1195.
(19) Zhang, Q.; Su, R.; Liu, X. F.; Xing, J.; Sum, T. C.; Xiong, Q. H. High-Quality Whispering-Gallery-Mode Lasing from Cesium Lead Halide Perocskite Nanoplatelets. *Adv. Funct. Mater.* **2016**, *26*, 6238−6245.
(20) Saidaminov, M. I.; Haque, M. A.; Savoie, M.; Abdelhady, A. L.; Cho, N.; Dursun, I.; Buttner, U.; Alarousu, E.; Wu, T.; Bakr, O. M. Perovskite Photodetectors Operating in Both Narrowband and Broadband Regimes. *Adv. Mater.* **2016**, *28*, 8144−8149.
(21) Sun, Z. H.; Aigouy, L.; Chen, Z. Y. Plasmonic-Enhanced Perovskite-Graphene Hybrid Photodetectors. *Nanoscale* **2016**, *8*, 7377−7383.
(22) Lu, J. W.; Sheng, X. X.; Tong, G. Q.; Yu, Z. W.; Sun, X. L.; Yu, L. W.; Xu, X. X.; Wang, J. Z.; Xu, J.; Shi, Y.; Chen, K. J. Ultrafast Solar-Blind Ultraviolet Detection by Inorganic Perovskite $CsPbX_3$ Quantum Dots Radial Junction Architecture. *Adv. Mater.* **2017**, *29*, 1700400.
(23) Tong, G. Q.; Geng, X. S.; Yu, Y. Q.; Yu, L. W.; Xu, J.; Jiang, Y.; Sheng, Y.; Shi, Y.; Chen, K. J. Rapid, Stable and Self-Powered Perovskite Detectors *via* a Fast Chemical Vapor Deposition Process. *RSC Adv.* **2017**, *7*, 18224−18230.
(24) Li, Y.; Shi, Z.; Lei, L.; Ma, Z.; Zhang, F.; Li, S.; Wu, D.; Xu, T.; Li, X.; Shan, C.; Du, G. Controllable Vapor-Phase Growth of Inorganic Perovskite Microwire Networks for High-Efficiency and Temperature-Stable Photodetectors. *ACS Photonics* **2018**, *5*, 2524−2532.
(25) Stoumpos, C. C.; Malliakas, C. D.; Peters, J. A.; Liu, Z. F.; Sebastian, M.; Im, J.; Chasapis, T. C.; Wibowo, A. C.; Chung, D. Y.; Freeman, A. J.; Wessels, B. W.; Kanatzidis, M. G. Crystal Growth of the Perovskite Semiconductor $CsPbBr_3$: A New Material for High-Energy Radiation Detection. *Cryst. Growth Des.* **2013**, *13*, 2722−2727.
(26) Chen, J.; Fu, Y. P.; Samad, L.; Dang, L.; Zhao, Y. Z.; Shen, S. H.; Guo, L. J.; Jin, S. Vapor-Phase Epitaxial Growth of Aligned Nanowire Networks of Cesium Lead Halide Perovskites. *Nano Lett.* **2017**, *17*, 460−466.
(27) Zhang, J.; Wang, Q.; Zhang, X. S.; Jiang, J. X.; Gao, Z. F.; Jin, Z. W.; Liu, S. Z. High-Performance Transparent Ultraviolet Photodetectors Based on Inorganic Perovskite $CsPbCl_3$ Nanocrystals. *RSC Adv.* **2017**, *7*, 36722−36727.
(28) Liu, X. H.; Yu, D. J.; Cao, F.; Li, X. M.; Ji, J. P.; Chen, J.; Song, X. F.; Zeng, H. B. Low-Voltage Photodetectors with High Responsivity Based on Solution-Processed Micrometer-Scale All-Inorganic Perovskite Nanoplatelets. *Small* **2017**, *13*, 1700364.
(29) Yang, B.; Zhang, F. Y.; Chen, J. S.; Yang, S. Q.; Xia, X. S.; Pullerits, T.; Deng, W. Q.; Han, K. L. Ultrasensitive and Fast All-Inorganic Perovskite-Based Photodetector *via* Fast Carrier Diffusion. *Adv. Mater.* **2017**, *29*, 1703758.
(30) Song, J. Z.; Xu, L. M.; Li, J. H.; Xue, J.; Dong, Y. H.; Li, X.; Zeng, H. B. Monolayer and Few-Layer All-Inorganic Perovskites as a New Family of Two-Dimensional Semiconductors for Printable Optoelectronic Devices. *Adv. Mater.* **2016**, *28*, 4861−4869.
(31) Tang, X. S.; Zu, Z. Q.; Shao, H. B.; Hu, W.; Zhou, M.; Deng, M.; Chen, W. W.; Zang, Z. G.; Zhu, T.; Xue, J. M. All-Inorganic Perovskite $CsPb(Br/I)_3$ Nanorods for Optoelectronic Application. *Nanoscale* **2016**, *8*, 15158−15161.
(32) Cheng, M.; Li, Y. Y.; Safdari, M.; Chen, C.; Liu, P.; Kloo, L.; Sun, C. L. Efficient Perovskite Solar Cells Based on a Solution Processable Nickel(II) Phthalocyanine and Vanadium Oxide Integrated Hole Transport Layer. *Adv. Energy Mater.* **2017**, *7*, 1602556.
(33) Xia, H. R.; Li, J.; Sun, W. T.; Peng, L. M. Organohalide Lead Perovskite Based Photodetectors with Much Enhanced Performance. *Chem. Commun.* **2014**, *50*, 13695−13697.
(34) Nefedov, V. I. X-ray Photoelectron Spectra of Halogens in Coordination Compounds. *J. Electron Spectrosc. Relat. Phenom.* **1977**, *12*, 459−476.
(35) Li, X. M.; Wu, Y.; Zhang, S. L.; Cai, B.; Gu, Y.; Song, J. Z.; Zeng, H. B. $CsPbX_3$ Quantum Dots for Lighting and Displays: Room-Temperature Synthesis, Photoluminescence Superiorities, Unsering Origins and White Light-Emitting Diodes. *Adv. Funct. Mater.* **2016**, *26*, 2435−2445.
(36) Shi, Z.; Li, S.; Li, Y.; Ji, H.; Li, X.; Wu, D.; Xu, T.; Chen, Y.; Tian, Y.; Zhang, Y.; Shan, C.; Du, G. Strategy of Solution-Processed All-Inorganic Heterostructure for Humidity/Temperature-Stable Perovskite Quantum Dot Light-Emitting Diodes. *ACS Nano* **2018**, *12*, 1462−1472.
(37) Wei, S.; Yang, Y. C.; Kang, X. J.; Wang, L.; Huang, L. J.; Pan, D. C. Room-Temperature and Gram-Scale Synthesis of $CsPbX_3$ (X = Cl, Br, I) Perovskite Nanocrystals with 50−85% Photoluminescence Quantum Yields. *Chem. Commun.* **2016**, *52*, 7265−7268.
(38) Leng, M. Y.; Yang, Y.; Zeng, K.; Chen, Z. W.; Tan, Z. F.; Li, S. R.; Li, J. H.; Xu, B.; Li, D. B.; Hautzinger, M. P.; Fu, Y. P.; Zhai, T. Y.;

DOI: 10.1021/acs.chemmater.8b02435
Chem. Mater. 2018, 30, 6744−6755

Xu, L.; Niu, G. D.; Tang, J. All-Inorganic Bismuth-Based Perovskite Quantum Dots with Bright Blue Photoluminescence and Excellent Stability. *Adv. Funct. Mater.* **2018**, *28*, 1704446.
(39) Li, X. M.; Wu, Y.; Zhang, S. L.; Cai, B.; Gu, Y.; Song, J. Z.; Zeng, H. B. $CsPbX_3$ Quantum Dots for Lighting and Displays: Room-Temperature Synthesis, Photoluminescece and White Light-Emitting Diodes. *Adv. Funct. Mater.* **2016**, *26*, 2435−2445.
(40) Xing, J.; Liu, X. F.; Zhang, Q.; Ha, S. T.; Yuan, Y. W.; Shen, C.; Sum, T. C.; Xiong, Q. H. Vapor Phase Synthesis of Organometyal Halide Perovskite Nanowires for Tunable Room-Temperature Nanolasers. *Nano Lett.* **2015**, *15*, 4571−4577.
(41) Lv, L.; Xu, Y.; Fang, H.; Luo, W.; Xu, F.; Liu, L.; Wang, B.; Zhang, X.; Yang, D.; Hu, W. D.; Dong, A. G. Generalized Colloidal Synthesis of High-Quality, Two-Dimensional Cesium Lead Halide Perovskite Nanosheets and Their Applications in Photodetectors. *Nanoscale* **2016**, *8*, 13589−13596.
(42) Shinde, A.; Gahlaut, R.; Mahamuni, S. Low Temperature Photoluminescence Studies of $CsPbBr_3$ Quantum Dots. *J. Phys. Chem. C* **2017**, *121*, 14872−14878.
(43) Dey, P.; Paul, J.; Bylsma, J.; Karaiskaj, D.; Luther, J. M.; Beard, M. C.; Romero, A. H. Origin of the Temperature Dependence of the Band Gap of PbS and PbSe Quantum Dots. *Solid State Commun.* **2013**, *165*, 49−54.
(44) Shi, D.; Du, M. H. Shallow Halogen Vacancies in Halide Optoelectronic Materials. *Phys. Rev. B: Condens. Matter Mater. Phys.* **2014**, *90*, 174103.
(45) Sebastian, M.; Peters, J. A.; Stoumpos, C. C.; Im, J.; Kostina, S. S.; Liu, Z.; Kanatzidis, M. G.; Freeman, A. J.; Wessels, B. W. Excitonic Emissions and Above-Band-Gap Luminescence in the Single-Crystal Perovskite Semiconductors $CsPbBr_3$ and $CsPbCl_3$. *Phys. Rev. B: Condens. Matter Mater. Phys.* **2015**, *92*, 235210.
(46) Ai, B.; Liu, C.; Deng, Z.; Wang, J.; Han, J.; Zhao, X. Low Temperature Photoluminescence Properties of $CsPbBr_3$ Quantum Dots Embedded in Glasses. *Phys. Chem. Chem. Phys.* **2017**, *19*, 17349−17355.
(47) Perumal, A.; Shendre, S.; Li, M.; Tay, Y. K. E.; Sharma, V. K.; Chen, S.; Wei, Z.; Liu, Q.; Gao, Y.; Buenconsejo, P. J. S.; Tan, S. T.; Gan, C. L.; Xiong, Q. H.; Sum, T. C.; Demir, H. V. High Brightness Formamidinium Lead Bromide Perovskite Nanocrystal Light Emitting Devices. *Sci. Rep.* **2016**, *6*, 36733.
(48) Shi, Z.; Sun, X.; Wu, D.; Xu, T.; Tian, Y.; Zhang, Y.; Li, X.; Du, G. Near-Infrared Random Lasing Realized in a Perovskite $CH_3NH_3PbI_3$ Thin Film. *J. Mater. Chem. C* **2016**, *4*, 8373−8379.
(49) Phuong, L. Q.; Yamada, Y.; Nagai, M.; Maruyama, N.; Wakamiya, A.; Kanemitsu, Y. Free Carriers *versus* Excitons in $CH_3NH_3PbI_3$ Perovskite Thin Films at Low Temperatures: Charge Transfer from the Orthorhombic Phase to the Tetragonal Phase. *J. Phys. Chem. Lett.* **2016**, *7*, 2316−2321.
(50) Jiang, D. S.; Jung, H.; Ploog, K. Temperature Dependence of Photoluminescence from GaAs Single and Multiple Quantum-Well Heterostructures Grown by Molecular-Beam Epitaxy. *J. Appl. Phys.* **1988**, *64*, 1371−1377.
(51) Tanaka, K.; Takahashi, T.; Ban, T.; Kondo, T.; Uchida, K.; Miura, N. Comparative Study on the Excitons in Lead-Halide-Based Perovskite-Type Crystals $CH_3NH_3PbBr_3$ $CH_3NH_3PbI_3$. *Solid State Commun.* **2003**, *127*, 619−623.
(52) Yantara, N.; Bhaumik, S.; Yan, F.; Sabba, D.; Dewi, H. A.; Mathews, N.; Boix, P. P.; Demir, H. V.; Mhaisalkar, S. Inorganic Halide Perovskite for Efficient Light-Emitting Diodes. *J. Phys. Chem. Lett.* **2015**, *6*, 4360−4364.
(53) Jones, M.; Lo, S. S.; Scholes, G. D. Signatures of Exciton Dynamics and Carrier Trapping in the Time-Resolved Photoluminescence of Colloidal CdSe Nanocrystals. *J. Phys. Chem. C* **2009**, *113*, 18632−18642.
(54) Ding, J. X.; Du, S. J.; Zhao, Y.; Zhang, X. J.; Zuo, Z. Y.; Cui, H. Z.; Zhan, X. Y.; Gu, Y. J.; Sun, H. Q. High-Quality Inorganic-Organic Perovskite $CH_3NH_3PbI_3$ Single Crystals for Photo-detector Applications. *J. Mater. Sci.* **2017**, *52*, 276−284.
(55) Cao, M.; Tian, J. Y.; Cai, Z.; Peng, L.; Yang, L.; Wei, D. C. Perovskite Heterojunction Based on $CH_3NH_3PbBr_3$ Single Crystal for High-Sensitive Self-Powered Photodetector. *Appl. Phys. Lett.* **2016**, *109*, 233303.
(56) Xia, H. R.; Li, J.; Sun, W. T.; Peng, L. M. Organohalide Lead Perovskite Based Photodetectors with Much Enhanced Performance. *Chem. Commun.* **2014**, *50*, 13695−13697.
(57) Wang, F.; Mei, J. J.; Wang, Y. P.; Zhang, L. G.; Zhao, H. F.; Zhao, D. X. Fast Photoconductive Response in Organometal Halide Perovskite Photodetectors. *ACS Appl. Mater. Interfaces* **2016**, *8*, 2840−2846.
(58) Deng, H.; Yang, X. K.; Dong, D. D.; Li, B.; Yang, D.; Yuan, S. J.; Qiao, K. K.; Cheng, Y. B.; Tang, J.; Song, H. S. Flexible and Semitransparent Organolead Triiodide Perovskite Network Photodetector Arrays with High Stability. *Nano Lett.* **2015**, *15*, 7963−7969.
(59) Deng, H.; Dong, D. D.; Qiao, K.; Bu, L.; Li, B.; Yang, D.; Wang, H. E.; Cheng, Y. B.; Zhao, Z. X.; Tang, J.; Song, H. S. Growth, Patterning and Alignment of Organolead Iodide Perovskite Nanowires for Optoelectronic Devices. *Nanoscale* **2015**, *7*, 4163−4170.
(60) Zhuo, S. F.; Zhang, J. F.; Shi, Y. M.; Huang, Y.; Zhang, B. Self-Template-Directed Synthesis of Porous Perovskite Nanowires at Room Temperature for High-Performance Visible-Light Photodetectors. *Angew. Chem.* **2015**, *127*, 5785.
(61) Dong, Y. H.; Gu, Y.; Zou, Y. S.; Song, J. Z.; Xu, L. M.; Li, J. H.; Xue, J.; Li, X. M.; Zeng, H. B. Improving All-Inorganic Perovskite Photodetectors by Preferred Orientation and Plasmonic Effect. *Small* **2016**, *12*, 5622−5632.
(62) Mir, W. J.; Livache, C.; Goubet, N.; Martinez, B.; Jagtap, A.; Chu, A.; Coutard, N.; Cruguel, H.; Barisien, T.; Ithurria, S.; Nag, A.; Dubertret, B.; Ouerghi, A.; Silly, M. G.; Lhuillier, E. Strategy to overcome Recombination Limited Photocurrent Generation in $CsPbX_3$ Nanoctystal Arrays. *Appl. Phys. Lett.* **2018**, *112*, 113503.
(63) Cao, F.; Yu, D. J.; Li, X. M.; Zhu, Y.; Sun, Z. G.; Shen, Y. L.; Wu, Y.; Wei, Y.; Zeng, H. B. Highly Stable and Flexible Photodetector Arrays Based on Low Dimensional $CsPbBr_3$ Microcrystals and On-Paper Pencil-Drawn Electrodes. *J. Mater. Chem. C* **2017**, *5*, 7441−7445.
(64) Li, X. M.; Yu, D.; Cao, F.; Gu, Y.; Wei, Y.; Wu, Y.; Song, J. Z.; Zeng, H. B. Healing All-Inorganic Perovskite Films *via* Recyclable Dissolution-Recyrstallization for Compact and Smooth Carrier Channels of Optoelectronic Devices with High Stability. *Adv. Funct. Mater.* **2016**, *26*, 5903−5912.
(65) Shi, Z.; Li, Y.; Li, S.; Li, X.; Wu, D.; Xu, T.; Tian, Y.; Chen, Y.; Zhang, Y.; Zhang, B.; Shan, C.; Du, G. Localized Surface Plasmon Enhanced All-Inorganic Perovskite Quantum Dot Light-Emitting Diodes Based on Coaxial Core/Shell Heterojunction Architecture. *Adv. Funct. Mater.* **2018**, *28*, 1707031.
(66) Mizusaki, J.; Arai, K.; Fueki, K. Ionic conoduction of the perovskite-type haides. *Solid State Ionics* **1983**, *11*, 203−211.
(67) Aitola, K.; Domanski, K.; Baena, J. P. C.; Sveinbjörnsson, K.; Saliba, M.; Abate, A.; Grätzel, M.; Kauppinen, E.; Johansson, E. M. J.; Tress, W.; Hagfeldt, A.; Boschloo, G. High-Performance Perovskite Photodetectors Based on Solution-Processed All-Inorganic $CsPbBr_3$ Thin Films. *Adv. Mater.* **2017**, *29*, 1606398.
(68) Liang, J.; Wang, C.; Wang, Y. R.; Xu, Z. R.; Lu, Z. P.; Ma, Y.; Zhu, H. F.; Hu, Y.; Xiao, C. C.; Yi, X.; Zhu, G. Y.; Lv, H. L.; Ma, L. B.; Chen, T.; Tie, Z. X.; Jin, Z.; Liu, J. All-Inorganic Perovskite Solar Cells. *J. Am. Chem. Soc.* **2016**, *138*, 15829−15832.
(69) Tian, W.; Zhou, H. P.; Li, L. Hybrid Organic-Inorganic Perovskite Photodetectors. *Small* **2017**, *13*, 1702107.

DOI: 10.1021/acs.chemmater.8b02435
Chem. Mater. 2018, 30, 6744−6755